Phase transition and electronic structure evolution of MoTe₂ induced by W substitution

Wencan Jin,[1,*] Theanne Schiros,[2] Yi Lin,[1] Junzhang Ma,[3] Rui Lou,[4] Zhongwei Dai,[5] Jie-Xiang Yu,[5] Daniel Rhodes,[6]
Jerzy T. Sadowski,[7] Xiao Tong,[7] Tian Qian,[3] Makoto Hashimoto,[8] Donghui Lu,[8] Jerry I. Dadap,[1] Shancai Wang,[4]
Elton J. G. Santos,[9] Jiadong Zang,[5] Karsten Pohl,[5] Hong Ding,[3] James Hone,[1] Luis Balicas,[6]
Abhay N. Pasupathy,[1,†] and Richard M. Osgood, Jr.[1,‡]

[1]*Columbia University, New York, New York 10027, USA*
[2]*Fashion Institute of Technology, New York, New York 10001, USA*
[3]*Beijing National Laboratory for Condensed Matter Physics, Institute of Physics, Chinese Academy of Sciences, Beijing 100190, China*
[4]*Department of Physics, Renmin University of China, Beijing 100872, China*
[5]*University of New Hampshire, Durham, New Hampshire 03824, USA*
[6]*Florida State University, Tallahassee, Florida 32306, USA*
[7]*Center for Functional Nanomaterials, Brookhaven National Laboratory, Upton, New York 11973, USA*
[8]*Stanford Synchrotron Radiation Lightsource, SLAC National Accelerator Laboratory, Menlo Park, California 94025, USA*
[9]*School of Mathematics and Physics, Queen's University Belfast, BT71NN Belfast, United Kingdom*

The transition-metal dichalcogenide compounds MoTe₂ and WTe₂ are polymorphic with both semiconducting and metallic phases. The thermodynamically stable phase of WTe₂ at room temperature is orthorhombic and metallic and displays a wide range of interesting phenomena including type-II Weyl fermions, titanic magnetoresistance and superconductivity in bulk, and quantum spin Hall insulator behavior in the monolayer case. On the other hand, the stable phase of MoTe₂ at room temperature is a trigonal prismatic semiconductor that has a direct gap in the monolayer with strong spin-orbit coupling. The alloy series $Mo_{1-x}W_xTe_2$ thus offers the possibility for tuning the structural and, consequently, electronic phases via tuning of the composition. Here, we report comprehensive studies of the electronic structure of $Mo_{1-x}W_xTe_2$ alloys using angle-resolved photoemission spectroscopy and first-principles calculations as a function of composition. At room temperature, we find a sharp boundary between the orthorhombic and the trigonal prismatic phases at $x = 0.10$ using structural characterization. We also show that by compositional tuning it is possible to control the band inversion in this series of compounds thus yielding important consequences for topological surface states.

DOI: 10.1103/PhysRevB.98.144114

I. INTRODUCTION

Transition-metal dichalcogenides [(TMDCs), MX_2, $M =$ Mo, W; $X =$ Se, Te] are polymorphic with different crystal structures, including a trigonal prismatic $2H$ phase [Fig. 1(a)], a monoclinic $1T'$ phase, and an orthorhombic T_d phase [Fig. 1(d)]. These phases provide an important platform for exploring exotic physics and novel device applications. The semiconducting $2H$-phase TMDCs in monolayer form consist of a layer of hexagonally arranged transition-metal atoms sandwiched between two layers of chalcogen atoms. In monolayer $2H$ TMDCs, the sizable direct band gap [1–3] and valley degree of freedom [4–6] make this phase remarkably appealing for electronics [7], and spin- and valleytronics devices [8,9]. Recently, the metallic $1T'$ and T_d phases have attracted interest due to the presence of band inversion in these phases, making them important candidates for realizing novel topological quantum phenomena. The semimetallic $1T'$

phase exhibits a distorted octahedral structure with an inclined stacking angle of $\sim 93.9°$, which retains a centrosymmetric $P2_1/m$ space group. In contrast, in the orthorhombic T_d phase, the stacking angle is exactly 90°, which breaks inversion symmetry (space-group $Pmn2_1$) [10]. The T_d phase displays a number of unique electronic properties in both the bulk and the monolayer forms. Bulk crystals of both T_d-WTe₂ [11,12] and T_d-MoTe₂ [13] display a large non-saturating magnetoresistance, possibly due to electron-hole compensation. Bulk T_d-WTe₂ [14], T_d-MoTe₂ [15,16], as well as some of their alloys [17] are also known to be type-II Weyl fermions. These type-II Weyl fermions are characterized by touching points between the electron and the hole pockets with strongly tilted Weyl cones [14] in the bulk and Fermi-arc states on the surface. A number of angle-resolved photoemission spectroscopy (ARPES) studies of the electronic structures of T_d-WTe₂ [18–20], MoTe₂ [21–24], and $Mo_xW_{1-x}Te_2$ on the W-rich side [25,26] have found evidence for these features. Finally, in monolayer form, the T_d TMDCs are two-dimensional topological insulators that display the quantum spin Hall effect [13,27].

The rich electronic phenomenology associated with the semiconducting and metallic phases of these compounds has spurred intense interest in achieving precise control of

---

*Current address: University of Michigan, Ann Arbor, Michigan 48109.

†apn2108@columbia.edu

‡osgood@columbia.edu
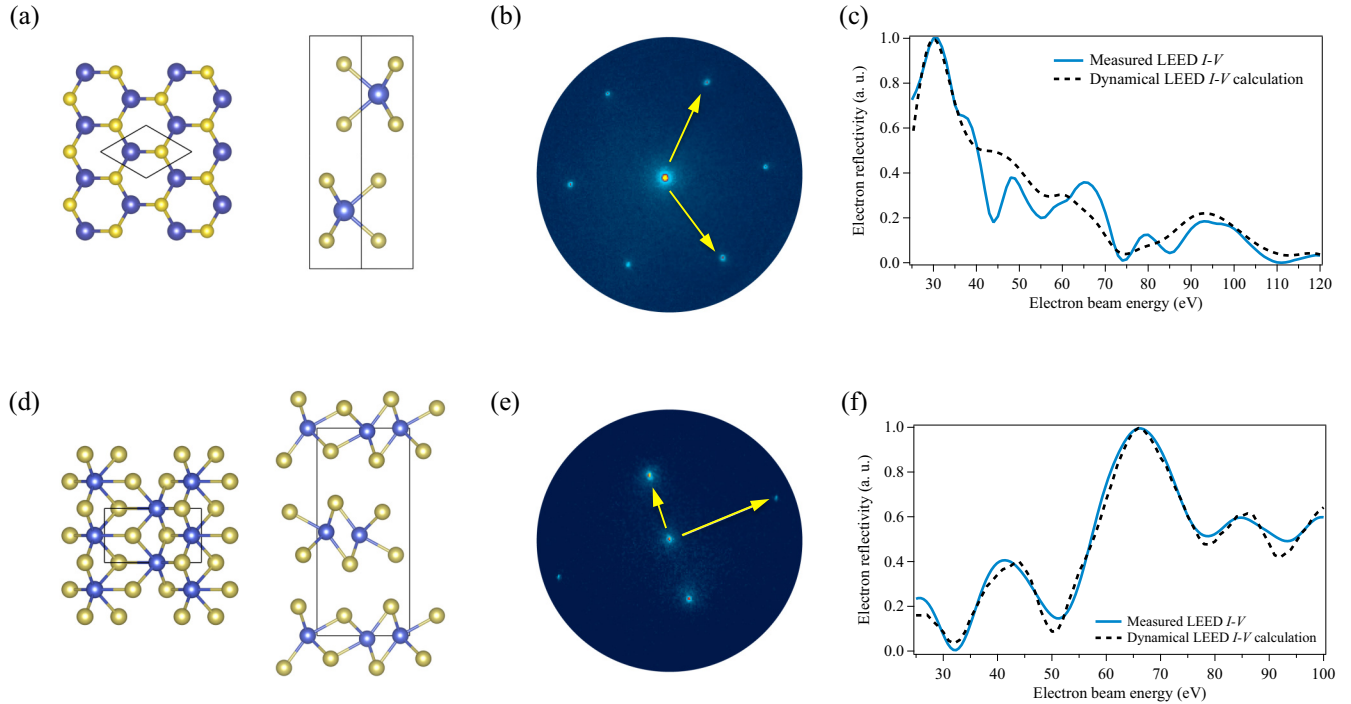
FIG. 1. Crystalline structure of $2H$- and T_d-$Mo_{1-x}W_x Te_2$ crystals. (a) A schematic of a $2H$-phase atomic structure in the top view (left) and side view (right), (b) low-energy electron diffraction (LEED) pattern, and (c) μ-LEED intensity-voltage (I-V) curve for $2H$-$Mo_{0.92}W_{0.08}Te_2$. (d) A schematic of the T_d-phase atomic structure in the top view (left) and side view (right), (e) LEED pattern, and (f) μ-LEED I-V curve for T_d-$Mo_{0.84}W_{0.16}Te_2$. The blue spheres: Mo/W atoms; the yellow spheres: Te atoms.

transitions between these phases. Such phase engineering of TMDCs has recently been attempted using a variety of tuning parameters, such as temperature, strain, chemical doping, and electrostatic doping [13,28–32]. Achieving reversible control of the phase transition is important for on-demand topological properties as well as for the development of technological applications, such as phase-change memory devices [33,34]. One of the chief difficulties in achieving this reversible control in the parent compounds $MoTe_2$ and WTe_2 is that the crystals are fairly stable at room temperature. In this context, alloying has been shown by some of us to play an important role in structural phase control [35]. Briefly, at room temperature, the thermodynamically stable phase of $MoTe_2$ is the semiconducting $2H$ polymorph. In contrast, the stable phase of WTe_2 is the semimetallic T_d polymorph. By using chemical alloying to produce the series $Mo_{1-x}W_x Te_2$, we showed the existence of a phase transition at around $x = 0.08$. We expect that as we approach the critical doping, the alloys become sensitive to dynamical tuning parameters, such as strain and electrostatic doping, opening up new possibilities for structural control. As we approach this critical doping, we must understand the electronic structures of the alloys on either side of the phase transition in detail. In this paper, we achieve understanding by performing synchrotron-based ARPES measurements of $Mo_{1-x}W_x Te_2$ as a function of W concentration, supported by structural characterization and density functional theory. The major findings of our paper show that: (i) the phase transition from $2H$ to T_d appears on the Mo-rich side (critical W concentration of $x_c \sim 0.10 \pm 0.01$) of the alloy composition point, in contrast to the previously predicted value of

0.33 [36]; (ii) W doping results in an upward shift of the conduction-band minimum (CBM), thus reducing the band inversion; and (iii) a demonstration via density functional theory (DFT) calculations that the interlayer coupling in this material is weaker than in the more widely studied TMDCs, such as MoS_2.

II. RESULTS AND DISCUSSION

The synthesis method for our crystals has been detailed in Ref. [35]. Prior to our ARPES measurements, the composition of the alloys was first determined with x-ray photoemission spectroscopy (XPS) (see the Supplemental Material [37]). The crystalline structure of $Mo_{1-x}W_x Te_2$ alloys was then investigated using selected-area low-energy electron diffraction (μ-LEED) at room temperature. The well-defined hexagonal μ-LEED pattern [see Fig. 1(b)], acquired from an $x = 0.08$ alloy, demonstrates that the alloys with $x < x_c$ crystallize in the $2H$ phase. In comparison, the rectangular μ-LEED pattern [Fig. 1(e)] for a crystal of composition of $x = 0.16$ shows that moderate W substitution ($x > x_c$) stabilizes the T_d phase at room temperature. Note that multiple locations were surveyed across the sample surface, and no phase coexistence was observed. In addition, to examine any major changes in crystal structure within the surface layers, the surface structures of these $Mo_{1-x}W_x Te_2$ alloys were determined using dynamical LEED calculations [38–40]. The optimized surface structures for the $2H$ and T_d phases were obtained by fitting the calculated I-V curves to the measured ones. Figures 1(c) and 1(f) show the measured LEED-I-V (blue solid curve) for the (00)
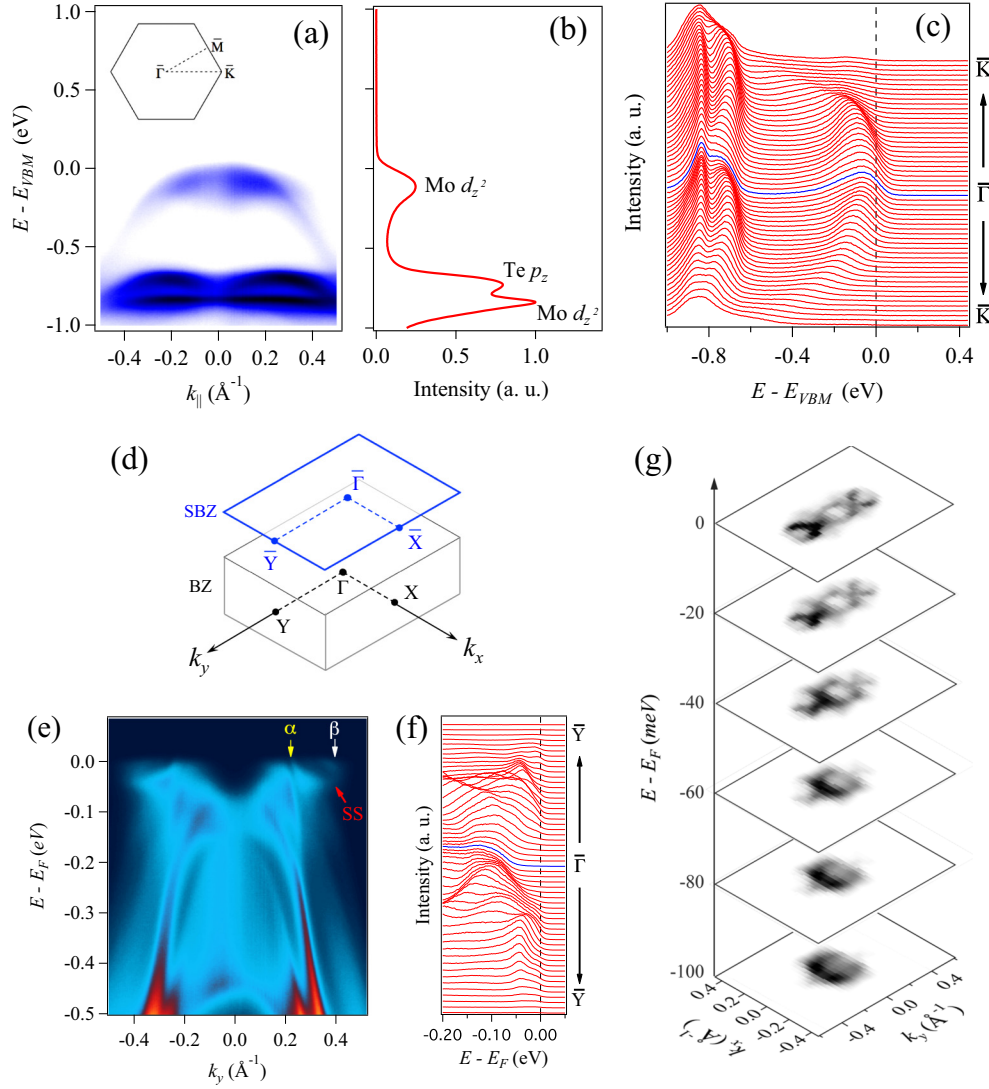
FIG. 2. Electron structure of $Mo_{1-x}W_xTe_2$ alloys across critical W concentrations. Electronic structure of the $2H$-$Mo_{0.94}W_{0.06}Te_2$ alloy. (a) An ARPES band map along the $\bar{K}$-$\bar{\Gamma}$-$\bar{K}$ high-symmetry direction, and the inset shows the surface Brillouin zone (SBZ). (b) An integrated spectrum, and (c) the energy distribution curve (EDC) plot of an ARPES band map shown in (a). The electronic structure of the T_d-$Mo_{0.80}W_{0.20}Te_2$ alloy, (d) the bulk BZ and projected (001) SBZ, (e) the ARPES band map ($h\nu = 24$ eV) along the $\bar{Y}$-$\bar{\Gamma}$-$\bar{Y}$ high-symmetry direction, (f) the EDC plot of the band features near the Fermi level (E_F), and (g) a stack of constant energy maps.

diffraction beam and the calculated I-V (black dashed curve). Despite the discrepancy between the calculated and the measured I-V curves in Fig. 1(c), which is largely due to the effect of atomic vibration and surface roughness, satisfactory Pendry R factors of 5.2% and 0.5% are obtained for the $2H$ and T_d cases, respectively, confirming a reliable determination of the surface structure. Our structural optimization indicated that the surface structure is distinct from that in the bulk by <5% relaxation, which is not significantly different enough to change the electronic structure.

ARPES measurements were then carried out to investigate the electronic structures of $Mo_{1-x}W_xTe_2$ alloys; to sharpen the spectra, the measurements were made at low temperatures. Figure 2(a) shows the ARPES band map of the $2H$-$Mo_{0.94}W_{0.06}Te_2$ alloy along the $\bar{K}$-$\bar{\Gamma}$-$\bar{K}$ high-symmetry direction of the surface Brillouin zone (see the inset). The corresponding integrated spectrum [Fig. 2(b)] shows that the

main band features are derived from the Mo d_{z^2} and Te p_z orbitals. The conduction bands were not observed up to 1 eV above the valence-band maximum (VBM), confirming that the $2H$ phase is semiconducting with a gap size of >1 eV. The band features are further displayed as corresponding EDC plots in Fig. 2(c). A parabolic fit of the topmost valence band yields a hole effective mass at $\bar{\Gamma}$ of $3.77m_0$ (where m_0 is the electron mass), which is larger than that of monolayer MoS_2 ($\sim 2.4m_0$). As revealed, the thickness-dependent electronic structure of MoS_2 [2], the topmost valence band at $\bar{\Gamma}$ decreases in energy with decreasing interlayer coupling strength, which leads to increasing hole effective mass. The remarkably flat topmost valence band implies rather weak interlayer coupling in the $2H$-$Mo_{0.94}W_{0.06}Te_2$ alloy.

In contrast to the semiconducting $2H$ phase, the ARPES band map [Fig. 2(e)] of the T_d phase ($x = 0.2$) along the $\bar{Y}$-$\bar{\Gamma}$-$\bar{Y}$ [Fig. 2(d)] high-symmetry direction shows a
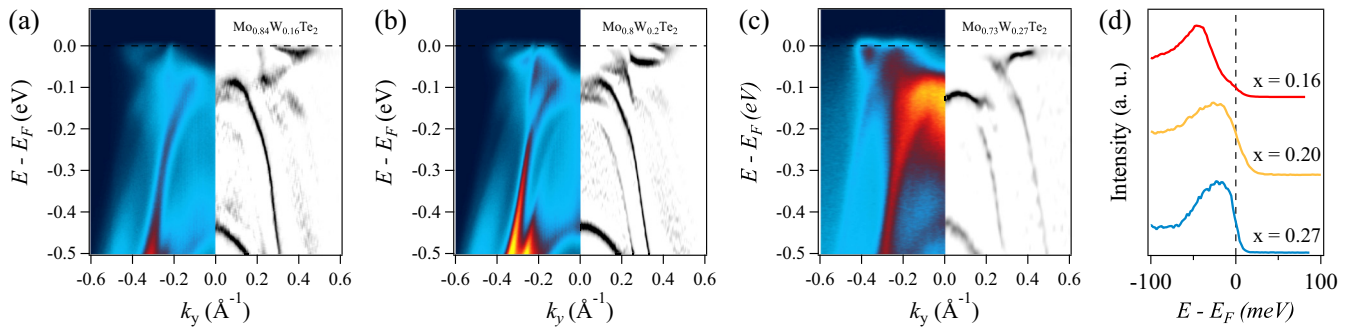
FIG. 3. Electronic structure evolution for different T_d-$Mo_{1-x}W_xTe_2$ alloys with W concentrations. ARPES band map (left) and corresponding second-derivative intensity plot (right) of T_d-$Mo_{1-x}W_xTe_2$ alloys along the $\bar{Y}$-$\bar{\Gamma}$-$\bar{Y}$ high-symmetry direction with (a) $x = 0.16$, (b) $x = 0.20$, and (c) $x = 0.27$. (d) Corresponding EDCs across the conduction-band minimum.

metallic nature in which a hole band (yellow arrow, α) and an electron pocket (white arrow, β) both cross the Fermi level. In addition, the surface state (red) protrudes into the electron pocket and almost overlaps with the hole band, which indicates that it is derived from a type-B surface [19]. These band features are further displayed in the EDC plot [Fig. 2(f)]. Figure 2(g) shows the stack of constant-energy maps. In particular, a palmier-shaped hole pocket and an almond-shaped electron pocket are observed in the Fermi-surface ($E = E_F$) map. The shapes of the hole and electron pockets are qualitatively in good agreement with those of WTe$_2$, MoTe$_2$, and Mo$_{1-x}$W$_x$Te$_2$ alloys. The sizes of the hole and electron pockets increase and decrease with increasing binding energy, respectively. We have comprehensively measured the electronic structure evolution of the T_d phase as a function of W concentrations. A side-by-side comparison of the electronic structure is made between $x = 0.16$, $x = 0.20$, and $x = 0.27$. As shown in the ARPES band maps and corresponding second derivative plots in Figs. 3(a)–3(c), the overlap in energy between valence and conduction bands decreases with increasing W concentration. Such an overlap can be characterized by the energy position of the CBM as shown in the EDC plots [Fig. 3(d)]. The CBM of $x = 0.16$ is located at $\sim$50 meV, which is comparable with that of pure T_d-MoTe$_2$ (60 meV) [21]. As the W concentration increases, the CBM shifts towards the Fermi level, and in the $x = 0.27$ alloy, the overlap is significantly suppressed, given the large content of Mo relative to W. Although we do not directly visualize the Weyl crossings in this data set, it is clear that the change in the band inversion also tunes the separation between the Weyl points and, consequently, the surface-state band structure.

To further investigate the band inversion observed here, we use density functional theory calculations to study the evolution of the electronic structure with alloying. Our previous photon energy-dependent ARPES studies [35] and theoretical calculations [41] have revealed that the dispersion along the k_z direction shows two-dimensional character. Here, we employ a model at the 2D limit by considering only one-unit-cell (1UC) thickness of the T_d structure [see Fig. 1(d)]. Figure 4(a) shows the calculated hole band and electron pocket as a function of W concentration. As the W concentration increases, the hole band slightly sinks, whereas the electron pocket rapidly shifts upwards. Our 1UC model captures the measured band inversion evolution very

well. This result further confirms the 2D character of the electronic structure. First-principles calculations can also give insight into the structural stability of the $2H$ and T_d phases as a function of alloying. To clarify this question, we first investigated both the $2H$ and the T_d phases of the bulk and monolayer structures of pure MoTe$_2$ and WTe$_2$. To directly compare the total energy between the $2H$ and the T_d phases with different W concentrations, we employ an expanded supercell containing 12(24) Mo/W atoms for 1UC (bulk) cases. This supercell can be regarded as a 3×2 supercell of the primitive cell for the T_d phase. The energy difference per Mo/W atom between $2H$ and T_d are shown in Fig. 4(b). The energy difference as a function of doping value x is nearly a linear relationship, which leads to a phase-transition point at $x = 0.25$ for bulk and $x = 0.13$ for the 1UC case. Here, the phase-transition point predicted by the bulk model is close to that of the previous study, whereas the 1UC model more accurately captures the measured critical doping value ($x_c \sim 0.10$), which further confirms that the Mo$_{1-x}$W$_x$Te$_2$ crystal is close to a 2D system rather than a van der Waals system.

III. CONCLUSION

In conclusion, we investigated the structural phase transition and electronic structure evolution of Mo$_{1-x}$W$_x$Te$_2$ alloys using ARPES and DFT calculations. Our results show that a critical W concentration of $x \sim 0.10$ triggers a phase transition from the $2H$ to the T_d phase, and in the T_d phase, topological strength is significantly suppressed by increasing W doping. The phase-transition point and electronic structure evolution are captured well by the DFT calculations using a 1UC model, indicating the 2D character of this material due to weak interlayer coupling.

IV. METHODS

Angle-resolved photoemission spectroscopy. ARPES measurements were performed, in part, at the Dreamline beamline of the Shanghai Synchrotron Radiation Facility with a Scienta D80 analyzer and, in part, at beamlines 5-2 and 5-4 of the Stanford Synchrotron Radiation Lightsource (SSRL) with Scienta R4000 and D80 analyzers, respectively. The energy and angular resolutions were set to better than 10 meV and 0.1°, respectively. The samples were measured between 30 and 60 K with a base pressure of $< 5 \times 10^{-11}$ Torr. The
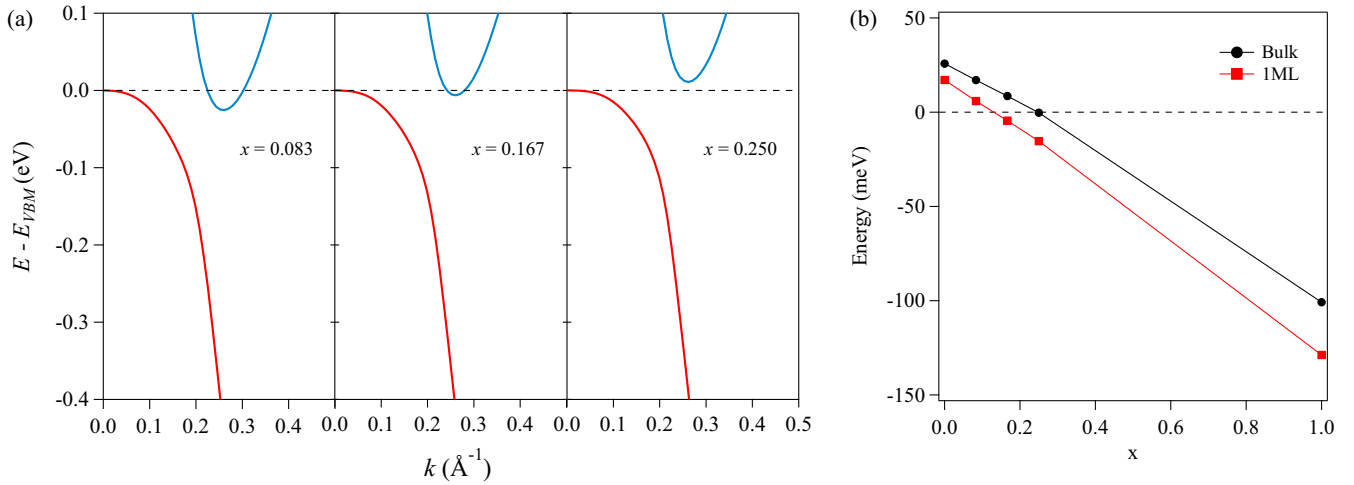
FIG. 4. (a) DFT calculated hole band and electron pocket with various W concentrations. The VBM is denoted by the dashed line. (b) The calculated energy difference between the $2H$ and the T_d phases as a function of doping value x of $Mo_{1-x}W_xTe_2$ for both bulk and 1UC.

ARPES data were collected within 12 h after cleavage during which time no signature of surface degradation was observed.

Low-energy electron microscopy. μ-LEED measurements were performed at the Center for Functional Nanomaterials, Brookhaven National Laboratory using an ELMITEC AC-LEEM (where LEEM represents low-energy electron microscopy) system. In this system, the sample was cleaved *in situ* at room temperature. The spatial resolution is <3 nm in the LEEM mode. The electron-beam spot size in the μ-LEED mode is 5 μm in diameter. LEED I-V curves are acquired by measuring the LEED intensity as a function of incident electron energies.

First-principles electronic structure calculation. The density functional theory calculation was carried out using a VASP package [42] with a projector-augmented plane-wave potential [43]. The exchange-correlation energy was described by the generalized gradient approximation in the form of Perdew *et al.* [44]. The Brillouin zone of the orthogonal unit cell of T_d-$Mo_{1-x}W_xTe_2$ was sampled by a $7 \times 12 \times 3$ k-point mesh. The energy cutoff was set to 440 eV. The van der Waals interactions were incorporated within the Tkatchenko-Scheffler method [45]. Spin-orbit coupling was also included for structural optimization. All structures were optimized until the atomic force on each atom, with both Hellmann-Feynman and van der Waals terms were taken into account, is less than 1 meV/Å. For the one-unit-cell case, a vacuum layer of 15 Å is used to build 2D slabs.

Dynamical LEED calculation. The codes from Adams [46], which were developed from the programs of Pendry and Alldredge [47] and Van Hove and Tong [48], were used in the dynamical LEED calculations. The lattice constants of WTe$_2$ are $a = 6.282$, $b = 3.496$, and $c = 14.07$ Å [49]. The lattice constants of MoTe$_2$ are $a = 6.335$, $b = 3.477$, and $c = 13.883$ Å [15]. As the lattice constant difference between MoTe$_2$ and WTe$_2$ is less than 1.5%, we use the weighted average as the lattice constants of the $Mo_{1-x}W_xTe_2$ alloys. The Debye temperature for $Mo_{1-x}W_xTe_2$ was set as 210 K. The inner potential of $Mo_{1-x}W_xTe_2$ is set as 10.1 eV. Twelve ($L = 11$) phase shifts are used in the calculation.

[1] K. F. Mak, C. Lee, J. Hone, J. Shan, and T. F. Heinz, Phys. Rev. Lett. **105**, 136805 (2010).

[2] W. Jin, P.-C. Yeh, N. Zaki, D. Zhang, J. T. Sadowski, A. Al-Mahboob, A. M. van Der Zande, D. A. Chenet, J. I. Dadap, I. P. Herman *et al.*, Phys. Rev. Lett. **111**, 106801 (2013).

[3] Y. Zhang, T.-R. Chang, B. Zhou, Y.-T. Cui, H. Yan, Z. Liu, F. Schmitt, J. Lee, R. Moore, Y. Chen *et al.*, Nat. Nanotechnol. **9**, 111 (2014).

[4] D. Xiao, G.-B. Liu, W. Feng, X. Xu, and W. Yao, Phys. Rev. Lett. **108**, 196802 (2012).

[5] K. F. Mak, K. He, J. Shan, and T. F. Heinz, Nat. Nanotechnol. **7**, 494 (2012).

[6] T. Cao, G. Wang, W. Han, H. Ye, C. Zhu, J. Shi, Q. Niu, P. Tan, E. Wang, B. Liu *et al.*, Nat. Commun. **3**, 887 (2012).

[7] Q. H. Wang, K. Kalantar-Zadeh, A. Kis, J. N. Coleman, and M. S. Strano, Nat. Nanotechnol. **7**, 699 (2012).

[8] K. F. Mak, K. L. McGill, J. Park, and P. L. McEuen, Science **344**, 1489 (2014).

[9] H. Zeng, J. Dai, W. Yao, D. Xiao, and X. Cui, Nat. Nanotechnol. **7**, 490 (2012).

[10] K. Zhang, C. Bao, Q. Gu, X. Ren, H. Zhang, K. Deng, Y. Wu, Y. Li, J. Feng, and S. Zhou, Nat. Commun. **7**, 13552 (2016).

[11] M. N. Ali, J. Xiong, S. Flynn, J. Tao, Q. D. Gibson, L. M. Schoop, T. Liang, N. Haldolaarachchige, M. Hirschberger, N. Ong *et al.*, Nature (London) **514**, 205 (2014).

[12] L. R. Thoutam, Y. L. Wang, Z. L. Xiao, S. Das, A. Luican-Mayer, R. Divan, G. W. Crabtree, and W. K. Kwok, Phys. Rev. Lett. **115**, 046602 (2015).

[13] D. H. Keum, S. Cho, J. H. Kim, D.-H. Choe, H.-J. Sung, M. Kan, H. Kang, J.-Y. Hwang, S. W. Kim, H. Yang *et al.*, Nat. Phys. **11**, 482 (2015).

[14] A. A. Soluyanov, D. Gresch, Z. Wang, Q. Wu, M. Troyer, X. Dai, and B. A. Bernevig, Nature (London) **527**, 495 (2015).

[15] Y. Sun, S.-C. Wu, M. N. Ali, C. Felser, and B. Yan, Phys. Rev. B **92**, 161107 (2015).

[16] Z. Wang, D. Gresch, A. A. Soluyanov, W. Xie, S. Kushwaha, X. Dai, M. Troyer, R. J. Cava, and B. A. Bernevig, Phys. Rev. Lett. **117**, 056805 (2016).

[17] T.-R. Chang, S.-Y. Xu, G. Chang, C.-C. Lee, S.-M. Huang, B. Wang, G. Bian, H. Zheng, D. S. Sanchez, I. Belopolski *et al.*, Nat. Commun. **7**, 10639 (2016).

[18] J. Sánchez-Barriga, M. G. Vergniory, D. Evtushinsky, I. Aguilera, A. Varykhalov, S. Blügel, and O. Rader, Phys. Rev. B **94**, 161401(R) (2016).

[19] F. Y. Bruno, A. Tamai, Q. Wu, I. Cucchi, C. Barreteau, A. De La Torre, S. M. Walker, S. Riccò, Z. Wang, T. Kim *et al.*, Phys. Rev. B **94**, 121112 (2016).

[20] C. Wang, Y. Zhang, J. Huang, S. Nie, G. Liu, A. Liang, Y. Zhang, B. Shen, J. Liu, C. Hu *et al.*, Phys. Rev. B **94**, 241119 (2016).

[21] K. Deng, G. Wan, P. Deng, K. Zhang, S. Ding, E. Wang, M. Yan, H. Huang, H. Zhang, Z. Xu, J. Denlinger, A. Fedorov, H. Yang, W. Duan, H. Yao, Y. Wu, S. Fan, H. Zhang, X. Chen, and S. Zhou, Nat. Phys. **12**, 1105 (2016).

[22] L. Huang, T. M. McCormick, M. Ochi, Z. Zhao, M.-T. Suzuki, R. Arita, Y. Wu, D. Mou, H. Cao, J. Yan, N. Trivedi, and A. Kaminski, Nature Mater. **15**, 1155 (2016).

[23] A. Tamai, Q. S. Wu, I. Cucchi, F. Y. Bruno, S. Riccò, T. K. Kim, M. Hoesch, C. Barreteau, E. Giannini, C. Besnard, A. A. Soluyanov, and F. Baumberger, Phys. Rev. X **6**, 031021 (2016).

[24] J. Jiang, Z. Liu, Y. Sun, H. Yang, C. Rajamathi, Y. Qi, L. Yang, C. Chen, H. Peng, C. Hwang *et al.*, Nat. Commun. **8**, 13973 (2017).

[25] I. Belopolski, D. S. Sanchez, Y. Ishida, X. Pan, P. Yu, S.-Y. Xu, G. Chang, T.-R. Chang, H. Zheng, N. Alidoust *et al.*, Nat. Commun. **7**, 13643 (2016).

[26] I. Belopolski, S.-Y. Xu, Y. Ishida, X. Pan, P. Yu, D. S. Sanchez, H. Zheng, M. Neupane, N. Alidoust, G. Chang *et al.*, Phys. Rev. B **94**, 085127 (2016).

[27] X. Qian, J. Liu, L. Fu, and J. Li, Science **346**, 1344 (2014).

[28] K.-A. N. Duerloo, Y. Li, and E. J. Reed, Nat. Commun. **5**, 4214 (2014).

[29] S. Cho, S. Kim, J. H. Kim, J. Zhao, J. Seok, D. H. Keum, J. Baik, D.-H. Choe, K. Chang, K. Suenaga *et al.*, Science **349**, 625 (2015).

[30] K.-A. N. Duerloo and E. J. Reed, ACS Nano **10**, 289 (2015).

[31] Y. Li, K.-A. N. Duerloo, K. Wauson, and E. J. Reed, Nat. Commun. **7**, 10671 (2016).

[32] Y. Wang, J. Xiao, H. Zhu, Y. Li, Y. Alsaid, K. Y. Fong, Y. Zhou, S. Wang, W. Shi, Y. Wang *et al.*, Nature (London) **550**, 487 (2017).

[33] M. Wuttig and N. Yamada, Nature Mater. **6**, 824 (2007).

[34] Q. Wang, E. T. Rogers, B. Gholipour, C.-M. Wang, G. Yuan, J. Teng, and N. I. Zheludev, Nat. Photonics **10**, 60 (2016).

[35] D. Rhodes, D. Chenet, B. Janicek, C. Nyby, Y. Lin, W. Jin, D. Edelberg, E. Mannebach, N. Finney, A. Antony *et al.*, Nano Lett. **17**, 1616 (2017).

[36] C. Zhang, S. KC, Y. Nie, C. Liang, W. G. Vandenberghe, R. C. Longo, Y. Zheng, F. Kong, S. Hong, R. M. Wallace *et al.*, ACS Nano **10**, 7370 (2016).

[37] See Supplemental Material at http://link.aps.org/supplemental/10.1103/PhysRevB.98.144114 for the determination of the stoichiometry of alloys using XPS.

[38] Z. Dai, W. Jin, M. Grady, J. T. Sadowski, J. I. Dadap, R. M. Osgood, and K. Pohl, Surf. Sci. **660**, 16 (2017).

[39] W. Jin, S. Vishwanath, J. Liu, L. Kong, R. Lou, Z. Dai, J. T. Sadowski, X. Liu, H.-H. Lien, A. Chaney *et al.*, Phys. Rev. X **7**, 041020 (2017).

[40] Z. Dai, W. Jin, J.-X. Yu, M. Grady, J. T. Sadowski, Y. D. Kim, J. Hone, J. I. Dadap, J. Zang, R. M. Osgood Jr. *et al.*, Phys. Rev. Mater. **1**, 074003 (2017).

[41] D. Rhodes, R. Schönemann, N. Aryal, Q. Zhou, Q. Zhang, E. Kampert, Y.-C. Chiu, Y. Lai, Y. Shimura, G. McCandless *et al.*, Phys. Rev. B **96**, 165134 (2017).

[42] G. Kresse and J. Furthmüller, Phys. Rev. B **54**, 11169 (1996).

[43] P. E. Blöchl, Phys. Rev. B **50**, 17953 (1994).

[44] J. P. Perdew, K. Burke, and M. Ernzerhof, Phys. Rev. Lett. **77**, 3865 (1996).

[45] A. Tkatchenko and M. Scheffler, Phys. Rev. Lett. **102**, 073005 (2009).

[46] D. L. Adams, Surf. Sci. **519**, 157 (2002).

[47] J. Pendry and G. P. Alldredge, Phys. Today **30**(2), 57 (1977).

[48] M. A. Van Hove and S. Y. Tong, *Surface Crystallography by LEED: Theory, Computation and Structural Results* (Springer, Berlin, Heidelberg, 2012) .

[49] B. E. Brown, Acta Crystallogr. **20**, 268 (1966).